Machine-learning-guided discovery of kagome superconductors YRu_3B_2 and $LuRu_3B_2$

Rose Albu Mustaf,[1,2,*] Sajilesh K. P.,[1,2,*] Sanu Mishra,[1,2] Junze Deng,[3] Yi Jiang,[4] Kaja H. Hiorth,[3] Eeli O. Lamponen,[3] Martin Gutierrez-Amigo,[3] Päivi Törmä,[3] Miguel A. L. Marques,[5] B. Andrei Bernevig,[4,6,7] and Emilia Morosan[1,2,†]

[1]*Department of Physics and Astronomy, Rice University, Houston, Texas 77005, USA*
[2]*Rice Center for Quantum Materials, Rice University, Houston, Texas 77005, USA*
[3]*Department of Applied Physics, Aalto University School of Science, FI-00076 Aalto, Finland*
[4]*Donostia International Physics Center (DIPC), Paseo Manuel de Lardizábal, 20018 San Sebastián, Spain*
[5]*Research Center Future Energy Materials and Systems of the University Alliance Ruhr and Interdisciplinary Centre for Advanced Materials Simulation, Ruhr University Bochum, Universitätsstraße 150, D-44801 Bochum, Germany*
[6]*Department of Physics, Princeton University, Princeton, New Jersey 08544, USA*
[7]*IKERBASQUE, Basque Foundation for Science, 48013 Bilbao, Spain*

(Received 17 December 2025; accepted 28 May 2026; published 17 June 2026)

We report the experimental discovery of bulk superconductivity in two kagome lattice compounds, YRu_3B_2 and $LuRu_3B_2$, which were predicted through machine-learning-accelerated high-throughput screening combined with first-principles calculations. These materials crystallize in the hexagonal $CeCo_3B_2$-type structure with planar kagome networks formed by Ru atoms. We observe superconducting critical temperatures of $T_c = 0.81$ K for YRu_3B_2 and $T_c = 0.95$ K for $LuRu_3B_2$, confirmed through magnetization, specific heat, and electrical transport measurements. Both compounds exhibit nearly 100% superconducting volume fractions, demonstrating bulk superconductivity. Compared with isostructural $LaRu_3Si_2$, YRu_3B_2 and $LuRu_3B_2$ show a more dispersive Ru local $d_{x^2-y^2}$ quasiflat band [and thus a reduced density of states (DOS) at E_F] together with an overall hardening of the phonon spectrum, both of which lower the electron-phonon coupling (EPC) constant λ. Meanwhile, the dominant real-space EPC between Ru local $d_{x^2-y^2}$ states and the low-frequency Ru in-plane local x branch remains nearly unchanged, indicating that the reduction of λ originates from the $d_{x^2-y^2}$ DOS reduction and the overall phonon hardening. Superfluid weight calculations show that conventional contributions dominate over quantum geometric effects due to the dispersive nature of bands near the Fermi level. This work demonstrates the effectiveness of integrating machine-learning screening, first-principles theory, and experimental synthesis for accelerating the discovery of new superconducting materials.

DOI: 10.1103/lpqj-7hyg

I. INTRODUCTION

During the century since superconductivity was discovered experimentally in Hg [1], serendipity has been the predominant way of finding new superconductors. Even after the theory of conventional superconductivity had been established by Bardeen, Cooper, and Schrieffer (BCS) [2], the new understanding of the role of electron-phonon correlations aided little in predicting novel superconducting materials and their critical parameters. New classes of unconventional superconductors, such as cuprates [3], pnictides [4], heavy fermion superconductors [5], organic superconductors [6], and very recently nickelates [7] or even the conventional superconductor MgB_2 [8], were serendipitous discoveries, and not the result of any theoretical prediction. One success of the theoretical prediction of superconductivity has been metallic hydrogen [9] and hydrides [10], which were conjectured to be the best candidates for high-temperature superconductivity, based on the strong bonds and the light mass of hydrogen. Remarkably, hydrides currently hold the record for the highest experimentally observed superconducting critical temperatures [11], although at extremely high pressures. These materials were theoretically predicted using first-principles calculations before their experimental synthesis and characterization. The successful prediction and subsequent verification of superconductivity in these hydrogen-rich compounds represents a paradigm shift in materials discovery, demonstrating the power of computational methods to guide experimental efforts toward new superconductors.

Despite the success of first-principles theories in understanding the properties of superconducting materials, the immense vastness of the materials space and the high computational expense of these calculations impose a fundamental bottleneck for materials discovery. To address this challenge, machine learning (ML) has recently emerged as a powerful

*These authors contributed equally to this work.
†Contact author: emorosan@rice.edu

approach capable of accelerating the prediction of new superconductors [12–16]. ML models offer a means to rapidly screen candidate materials, which can then be strategically combined with conceptual guidelines derived from established theory, such as the identification of specific lattice motifs or structural features, for targeted searches. This ML-accelerated, theory-guided approach can be used to predict superconductivity in promising classes of materials, thereby guiding subsequent experimental synthesis and investigation.

In this context, materials with kagome lattices host quasi-flat bands with a large density of states, and have thus been a promising candidate for superconductivity. Flat bands with attractive interactions need quantum geometry [17] to enable supercurrent in flat bands [18,19], while with repulsive interactions, partially filled flat bands predominantly magnetize [20]. Recently, we conducted a comprehensive, *ab initio* investigation into the superconductivity of the flat-band kagome metal $LaRu_3Si_2$ [14]. Furthermore, we performed an ML-accelerated high-throughput screening of the entire 1:3:2 kagome family and identified several stable materials predicted to exhibit superconductivity.

Here, we present the successful experimental confirmation of bulk superconductivity in one of these predicted systems, YRu_3B_2, consistent with two other simultaneous reports [21,22]. In addition, we report a second isostructural superconductor, $LuRu_3B_2$. The Lu compound was initially overlooked in our high-throughput predictions [14] because its calculated phonon spectrum exhibits weakly imaginary modes, indicating a possible low-temperature dynamical instability. Although YRu_3B_2 and $LuRu_3B_2$ have been known for decades, their properties have not been explored below 1.2 K [23,24]. In this work, we report a detailed characterization of the bulk superconducting properties of these materials. Although the predicted critical temperatures (T_c) are higher (3.37 K for YRu_3B_2 and 1.88 K for $LuRu_3B_2$) than the experimental observations (0.81 and 0.95 K, respectively), this result clearly demonstrates the merit of combining ML-driven screening with refined, postscreening *ab initio* calculations and experiments. This integrated approach provides a useful pathway from theoretical prediction to experimental realization of novel superconducting materials.

II. EXPERIMENTS

A. Methods

$R\mathrm{Ru_3B_2}$ (R = Y, Lu) samples were prepared from high-purity elements (Y 99.99%, Lu 99.99%, Ru 99.99%, and B 99.99%) in a stoichiometric composition 1:3:2. The elements were arc melted on a water-cooled copper hearth in an argon atmosphere and remelted several times to ensure homogeneity. The mass loss during the melting process was negligible. The crystal structure was confirmed using powder x-ray diffraction in a Bruker D8 Advance diffractometer with Cu Kα radiation. Rietveld refinements were performed using FullProf suite software [25]. Magnetization measurements $M(T; H)$ were performed in a Quantum Design (QD) Magnetic Property Measurement System equipped with the iQuantum Helium-3 option. Specific heat $C_p(T; H)$ measurements were performed in a QD Dynacool Physical Property Measurement System with a dilution refrigerator option.

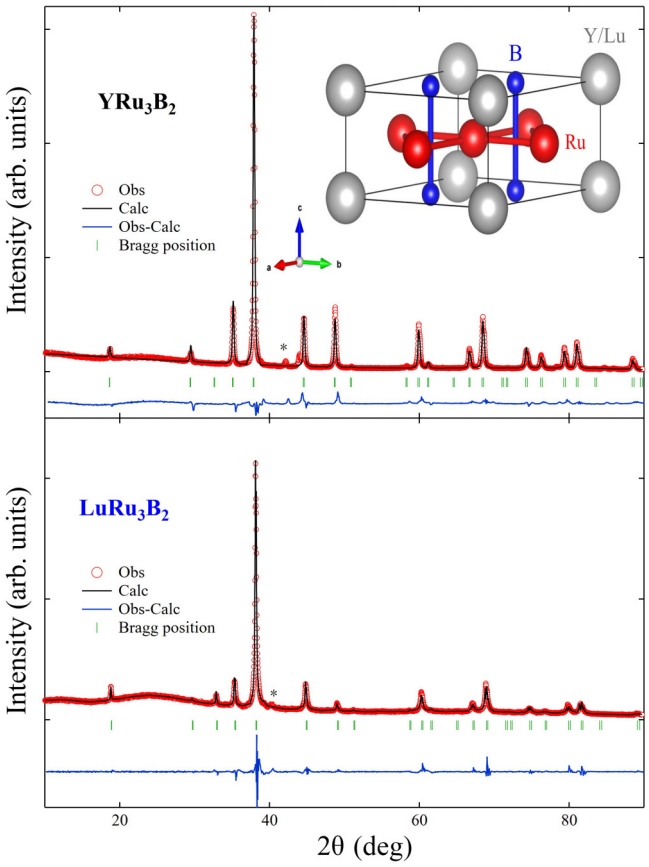

FIG. 1. Powder x-ray pattern for $R\mathrm{Ru_3B_2}$ (red), with calculated pattern (black) and Bragg peak positions (green ticks) for space group *P6/mmm*. The asterisk denotes residual Ru. Inset: Crystallographic unit cell of $R\mathrm{Ru_3B_2}$.

B. Results and discussion

$R\mathrm{Ru_3B_2}$ (R = Y, Lu) forms in the $CeCo_3B_2$-type structure, which crystallizes in the hexagonal *P6/mmm* space group (No. 191). In this structure, the Ru atoms arrange into a planar kagome network in the *ab* plane. The unit cell of $R\mathrm{Ru_3B_2}$ is shown in the inset of Fig. 1. Powder x-ray diffraction confirms the crystal structure and phase purity of the synthesized samples. The measured patterns (shown in Fig. 1) can be fit to the expected $CeCo_3B_2$ structure, with the exception of a minute peak corresponding to elemental Ru, marked by an asterisk. Rietveld refinement of the patterns for the two compounds yields lattice parameters of a = 5.475 Å and c = 3.027 Å for YRu_3B_2 and a = 5.448 Å and c = 3.014 Å for $LuRu_3B_2$.

We confirmed experimentally the superconductivity in YRu_3B_2 (black) and $LuRu_3B_2$ (blue) with thermodynamic and transport measurements (Figs. 2–5). The zero-field-cooled (ZFC) magnetization was measured on warming, with a small applied field H = 5 Oe. The measured susceptibility data $\chi = M/H$ were scaled by 4π and corrected for demagnetizing effects, where $4\pi\chi_{\mathrm{eff}} = 4\pi\chi/(1 - N_d\chi)$. A demagnetizing factor $N_d = 1/3$ was used for a nearly spherical sample morphology. The resulting superconducting fraction is close to 100% and 90%, respectively, in YRu_3B_2 and $LuRu_3B_2$, confirming the bulk superconducting state in both compounds. For an applied field H = 5 Oe, the critical

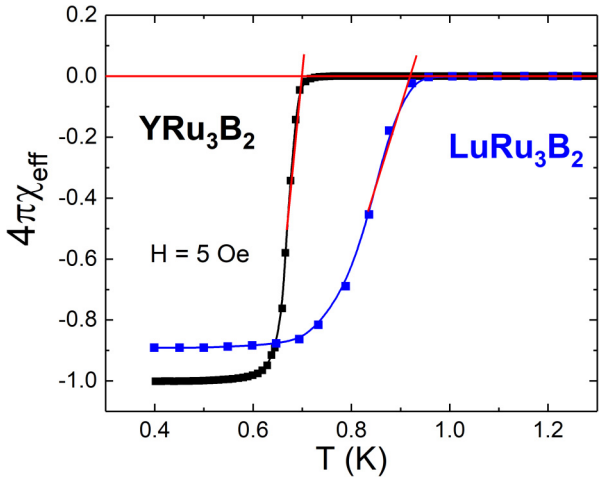

FIG. 2. ZFC magnetic susceptibility, $4\pi\chi_{\rm eff}$, as a function of temperature for YRu_3B_2 (black) and $LuRu_3B_2$ (blue) at $H = 5$ Oe.

temperatures, determined by the onset of diamagnetism in Fig. 2, are $T_c = 0.70$ K (YRu_3B_2) and 0.93 K ($LuRu_3B_2$). The critical field values can be estimated from the low-temperature magnetization isotherms $M(H)$ ($T = 0.4$ K) shown in Fig. 3. A linear fit of the low-H magnetization gives an estimate of the lower critical field H_{c1}, taken as the H value where $M(H)$ deviates from linearity (vertical arrow, inset). H_{c1} is close to 35 and 48 Oe for YRu_3B_2 (black) and $LuRu_3B_2$ (blue) compounds, respectively. In the $T = 0$ limit, $H_{c1}(0)$ can be estimated for both compounds, using [1]

$$H_{c1}(T) = H_{c1}(0)[1 - (T/T_c)^2]. \quad (1)$$

This gives $H_{c1}(0) = 52$ and 59 Oe for YRu_3B_2 and $LuRu_3B_2$, respectively. The upper critical field H_{c2} is determined as the field where $M(H)$ approaches zero (vertical arrows, Fig. 3). At $T = 0.4$ K, H_{c2} is close to 530 Oe for YRu_3B_2 and close to 660 Oe for $LuRu_3B_2$. Both of these values are consistent with the findings from specific heat (discussed below).

We were able to trace the superconducting state to lower temperatures and higher fields in specific heat (Fig. 4) measured down to $T = 60$ mK and applied magnetic field up to 800 Oe. A sharp jump was observed in the $H = 0$ specific heat at $T_c = 0.81$ and 0.95 K, respectively, for YRu_3B_2 and $LuRu_3B_2$. The superconducting transition temperature at each field value was determined from the equal entropy construct [with an example shown for $H = 0$ in Figs. 4(c) and 4(d)]. Given that magnetic susceptibility was measured in a small applied field, the specific heat T_c values of $H = 0$ are slightly higher because, as expected, the increasing applied magnetic field suppresses T_c (Fig. 4). The normal-state specific heat data for both samples can be modeled by the relation $C_p/T = \gamma_n + \beta T^2$, where γ_n and β represent the electronic and phononic coefficients, respectively. The fitting parameters for $H = 0$ are determined as $\gamma_n = 15.1\,\mathrm{mJ/(mol\,K)^2}$, $\beta = 0.16\,\mathrm{mJ/(mol\,K)^4}$ for the YRu_3B_2 sample, and $\gamma_n = 15.2\ \mathrm{mJ/(mol\,K)^2}$, $\beta = 0.48\,\mathrm{mJ/(mol\,K)^4}$ for the $LuRu_3B_2$ sample. The superconducting electronic specific heat coefficient γ_e can be estimated using γ_n and the residual electronic specific heat coefficient $\gamma_{\rm res}$, with the latter estimated from C_e/T at $T = 60$ mK and $H = 0$ (Fig. 4). Given that $\gamma_{\rm res}$ is much smaller than γ_n for both compounds, we approximate the electronic specific heat coefficient $\gamma_e = \gamma_n - \gamma_{\rm res} \sim \gamma_n$ for both YRu_3B_2 and $LuRu_3B_2$.

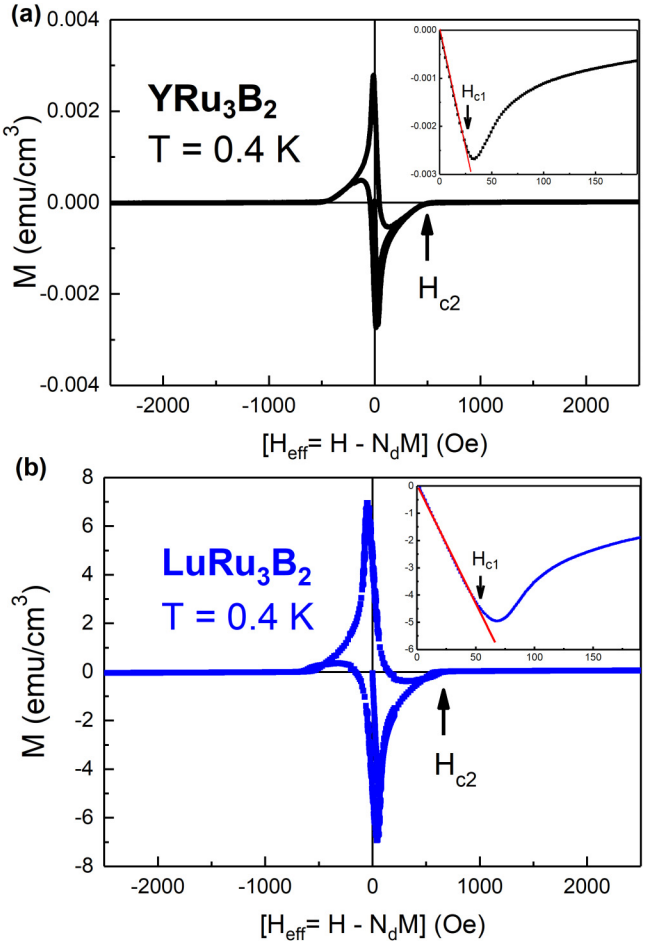

FIG. 3. Magnetization for (a) YRu_3B_2 and (b) $LuRu_3B_2$ as a function of $H_{\rm eff}$ at $T = 0.4$ K, where $H_{\rm eff} = H - N_d\,M$. Inset: Linear fit of the low-H magnetization showing where $M(H)$ deviates from linearity, giving an estimate for H_{c1}.

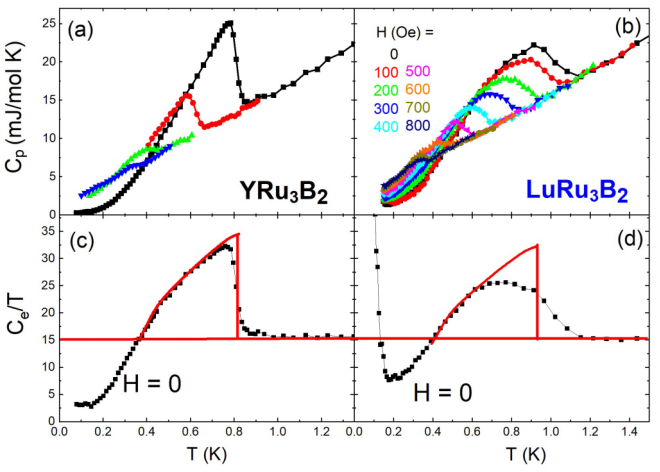

FIG. 4. $C_p(T)$ data for (a) YRu_3B_2 and (b) $LuRu_3B_2$ in applied fields ranging from 0 to 800 Oe.

TABLE I. Summary of parameters describing YRu_3B_2 and $LuRu_3B_2$ properties.

Compound	T_c (K)	$H_{c1}(0)$, $H_{c2}(0)$ (Oe)	γ_n (mJ/(mol K)^2)	β	$\Delta C_e/\gamma_n T_c$	$\lambda_{\text{e-ph}}^{\text{exp}}$ (m_e)	m^* (mJ/(mol K)^4)	$\lambda_L^{\text{exp}}(0)$ (nm)	$\lambda_L^{\text{th}}(0)$ (nm)
YRu_3B_2	0.81	52, 1000	15.1	0.16	1.1	0.41	1.41	32.3	32
$LuRu_3B_2$	0.95	59, 867	15.2	0.48	1.26	0.45	1.45	32.5	36

The $H = 0$ entropy-conservation construct shown in Figs. 4(c) and 4(d) for YRu_3B_2 and $LuRu_3B_2$, respectively, produces values for the jump in the electronic specific heat C_e at T_c, $\Delta C_e/\gamma T_c \sim 1.1$ and 1.26. This value is close to, albeit slightly lower than, the BCS predicted value of 1.43. This deviation can arise for a number of reasons, such as grain boundary effects (expected especially in polycrystalline samples) and non-BCS gap features, such as anisotropic or nodal superconducting gap. Our mean-field calculation based on a tight-binding model constructed from density functional theory (DFT) band structure calculation gives pairing gaps nonuniform among the orbitals, as described in Sec. III D. An upturn in the C_e/T for the Lu compound [Fig. 4(d)] is likely due to a nuclear Schottky anomaly at the low temperatures. Using the experimental β values, along with the universal gas constant R, and considering $N = 6$ atoms per unit cell, the Debye temperature (θ_D) can be calculated as $\theta_D = (12\pi^4 RN/5\beta)^{1/3}$. The Debye temperature turns out to be 418 K for YRu_3B_2 and 290 K for the $LuRu_3B_2$ compound. The electron-phonon coupling constant in these materials is determined using the following relation:

$$\lambda_{\text{e-ph}}^{\text{exp}} = \frac{1.04 + \mu^* \ln(\theta_D/1.45T_c)}{(1 - 0.62\mu^*)\ln(\theta_D/1.45T_c) - 1.04}. \quad (2)$$

Here, μ^* is the repulsive Coulomb interaction term, which is generally considered 0.13 for intermetallic samples. Substituting the values of θ_D and T_c yields $\lambda_{\text{e-ph}}^{\text{exp}} = 0.41$ (for YRu_3B_2) and 0.45 (for $LuRu_3B_2$), indicating the weakly coupled nature of superconductivity in both compounds. The electron-phonon coupling obtained from DFT calculations (Sec. III B) is $\lambda_{\text{e-ph}}^{\text{th}} = 0.477$ and 0.561 for the Y and Lu compounds, respectively, very close to the estimates from the experiment.

The Sommerfeld specific heat coefficient γ allows us to estimate the ideal London penetration depth $\lambda_L^{\text{exp}}(0)$: $\lambda_L(0) = (m^*/\mu_0 ne^2)^{1/2}$, where m^* is the electron effective mass scaled by the bare electron mass m_e, $m^*/m_e = (1 + \lambda_{\text{e-ph}}^{\text{exp}})$, and n is the carrier concentration. Due to the absence of single crystals that are required for Hall measurements and therefore experimental n estimates, we calculate the carrier concentration as $n = 3/V$, with V the unit cell volume determined experimentally from x-ray diffraction refinements. The value in the numerator here corresponds to the three electrons contributed by the trivalent ions Y^{3+} and Lu^{3+} in the two compounds. This yields $n = 3.82 \times 10^{-2}$ Å^{-3} and 3.87×10^{-2} Å^{-3} for YRu_3B_2 and $LuRu_3B_2$, respectively. The effective masses are $m^* = 1.41m_e$ and $1.45m_e$ for the Y and Lu compounds, respectively. Using these estimates, we can determine $\lambda_L^{\text{exp}}(0) =$ 32.3 nm (Y) and 32.5 nm (Lu). We have calculated the superfluid weight (superfluid stiffness) from DFT data (described in Sec. III E) and obtained the theoretical London penetration depth $\lambda_L^{\text{th}}(0) = 32$ nm (Y) and 36 nm (Lu) in the xy plane, and these are in good agreement with the experimental values. The superconducting properties for YRu_3B_2 and $LuRu_3B_2$ compounds are summarized in Table I.

The electrical resistivity measurements show metallic behavior for both samples, with residual resistivity ratios RRR $= \rho(300\,\text{K})/\rho_0$ of 6.8 and 5, respectively, for YRu_3B_2 and $LuRu_3B_2$ (Fig. 5). In the low-temperature range, the superconducting transition is observed, with the $H = 0$ resistivity reaching 0 around 0.84 K (YRu_3B_2) and 1.04 K ($LuRu_3B_2$), coinciding with thermodynamic measurements. The insets in Fig. 5 show the expected suppression of the superconducting temperature with applied field. The superconducting transition at each field is defined by the temperature at which the resistance reaches zero. From transport measurements, we can determine the residual resistivity ρ_0 to estimate the mean free path l_0 for both compounds:

$$l_0 = \frac{3\pi^2\hbar^3}{e^2 m^{*2}\rho_0 v_F^2}, \quad (3)$$

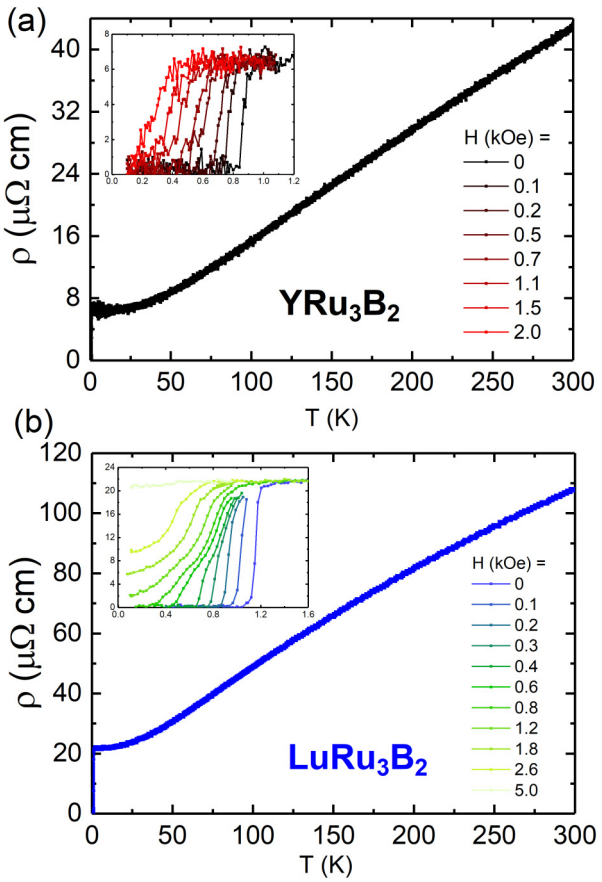

FIG. 5. $\rho(T)$ data for (a) YRu_3B_2 and (b) $LuRu_3B_2$ at zero field in the range 50 mK to 300 K. The insets show the superconducting transitions captured at different applied fields.

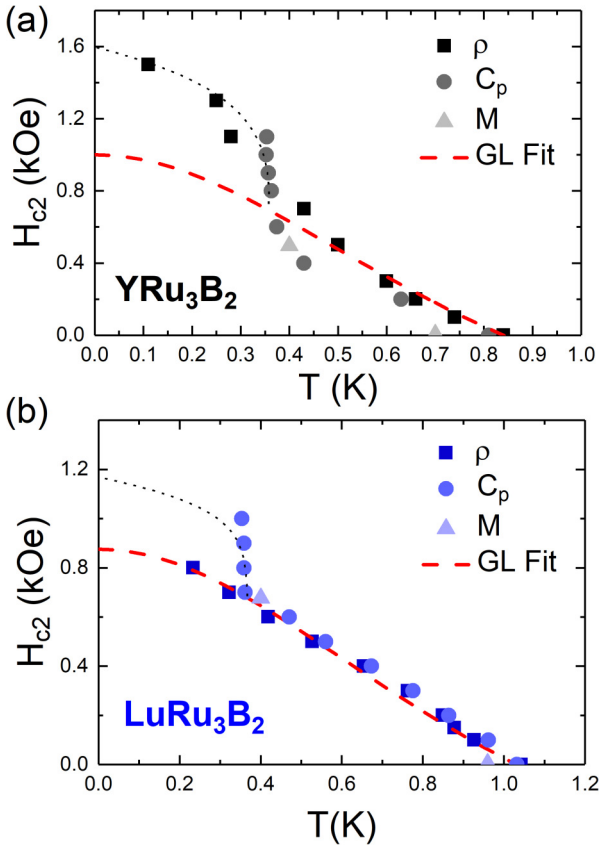

FIG. 6. $H_{c2}(T)$ phase diagram for (a) YRu_3B_2 and (b) $LuRu_3B_2$, with the GL fit [Eq. (5)] shown in red.

where the Fermi velocity v_F is calculated from

$$v_F = \frac{\hbar}{m^*}(3\pi^2 n)^{1/3}. \tag{4}$$

This gives a mean free path $l_0 = 17.9$ nm for YRu_3B_2 and 5.3 nm for $LuRu_3B_2$. Figure 6 shows the H_{c2}–T phase diagram for YRu_3B_2 [panel (a), black] and $LuRu_3B_2$ [panel (b), blue], constructed from resistivity (squares), heat capacity (circles), and magnetization (triangles) measurements. The $H_{c2}(0)$ critical field values for the two compounds are determined from the Ginzburg-Landau (GL) fits [1] (red dashed lines):

$$H_{c2}(T) = H_{c2}(0)\frac{1-(T/T_c)^2}{1+(T/T_c)^2}. \tag{5}$$

The resulting $H_{c2}(0)$ values are close to 1 and 0.87 kOe for YRu_3B_2 and $LuRu_3B_2$, respectively. It appears that the superconducting state cannot be described by a simple GL picture, as the H_{c2}–T phase diagram deviates from the conventional predicted behavior in both compounds. (The nearly field-independent nature of the heat capacity curves at high fields is shown in Fig. S1 of the Supplemental Material [26].) The black dotted line at low temperatures is a guide to the eye and gives approximate critical field values around 1.6 and 1.2 kOe at $T = 0$ K for YRu_3B_2 and $LuRu_3B_2$, respectively. Similar H_{c2}–T phase diagrams have previously been reported in $YbSb_2$ [27], KFe_2As_2 [28], single-layer $NbSe_2$ [29], UPt_3 [30], UTe_2 [31,32], and other heavy fermion superconductors, and have been attributed to a number of possible effects: multiband or multigap superconductivity, a superconducting state with a multicomponent order parameter, intrinsic structural or electronic inhomogeneity, or internal strain. Resolving the exact origin of the H_{c2} behavior at low temperatures in YRu_3B_2 and $LuRu_3B_2$ is left to a future study based on detailed theoretical calculations and experimental probes (including ac susceptibility, muon spin rotation and relaxation, optical measurements, or scanning tunneling microscopy).

We estimated the effective coherence length $\xi_{\text{eff}}(0)$ for both compounds using

$$H_{c2}(0) = \frac{\Phi_0}{2\pi\xi_{\text{eff}}(0)^2}, \tag{6}$$

where the flux quantum $\Phi_0 = 2.07 \times 10^{-15}$ Wb [1]. This gives $\xi_{\text{eff}}(0) = 57.3$ and 61.6 nm for YRu_3B_2 and $LuRu_3B_2$, respectively. To assess whether the material is in the clean or dirty limit, we evaluate the ratio of the BCS coherence length to the mean free path ξ_0/l_0, where ξ_0 can be found from

$$\xi_{\text{eff}}(0) = 0.855\sqrt{\xi_0 l_0}. \tag{7}$$

This yields ξ_0 values of 251 nm for YRu_3B_2 and 982 nm for $LuRu_3B_2$, suggesting that both systems fall in the dirty limit where $\xi_0 \gg l_0$. The effective penetration depth $\lambda_{\text{eff}}(0)$ can be determined from

$$H_{c1}(0) = \frac{\Phi_0}{4\pi\lambda_{\text{eff}}(0)^2}\ln\left(\frac{\lambda_{\text{eff}}(0)}{\xi_{\text{eff}}(0)}\right). \tag{8}$$

This gives $\lambda_{\text{eff}}(0) = 198.1$ and 166.6 nm for YRu_3B_2 and $LuRu_3B_2$, respectively. These values are larger than the ideal London penetration depth $\lambda_L(0)$, which can occur, for example, due to disorder and nonlocal effects as well as from the simplified approximations inherent in both theoretical descriptions. In addition, the analysis in Sec. III E shows that, although quasiflat bands exist in the band structure, the superfluid weight is mostly conventional; the geometric contribution is small because the dispersion of the bands at the Fermi level is large compared to the small superconducting order parameters for these low-temperature superconductors.

III. THEORY

A. Methods

First-principles calculations were carried out within DFT using the projector augmented-wave method [33,34], as implemented in the Vienna *ab initio* simulation package [35,36]. The exchange-correlation potential was treated within the generalized gradient approximation (GGA) using the Perdew-Burke-Ernzerhof (PBE) functional [37]. A plane-wave energy cutoff of 500 eV was used, and the Brillouin zone was sampled with a Γ-centered Monkhorst-Pack **k**-point grid of $12 \times 12 \times 12$ [38]. Irreducible representations of the electronic states were obtained using IRVSP [39]. Maximally localized Wannier functions (MLWFs) were constructed for *R*-*s*, *d*, Ru-*s*, *d*, and B-*s*, *p* orbitals in local basis [40–44]. Based on these MLWFs, the Fermi surfaces, density of states, and orbital-resolved band structures were computed using WANNIERTOOLS [45].

Phonon spectra were calculated via the QUANTUM ESPRESSO package in the framework of density functional

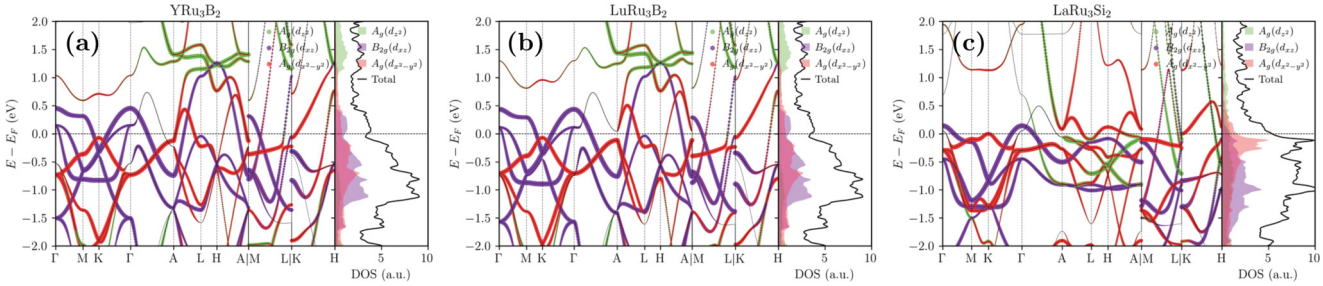

FIG. 7. Orbital-projected band structure and DOS of the $P6/mmm$ structure for (a) YRu_3B_2, (b) $LuRu_3B_2$, and (c) $LaRu_3Si_2$. The d orbitals (specifically d_{z^2}, $d_{x^2-y^2}$, and d_{xz}) of Ru atoms are projected onto the band structure, with the radius of the circles proportional to the projected weight.

perturbation theory (DFPT). Electron-phonon coupling (EPC) properties were computed using the EPW package [46–49], included within QUANTUM ESPRESSO [50,51]. Electron-phonon matrix elements were first computed on coarse **k**-point and **q**-point meshes ($8 \times 8 \times 12$ and $4 \times 4 \times 4$) and then interpolated onto finer grids ($32 \times 32 \times 32$) using maximally localized Wannier functions.

Superfluid weight calculations were performed using the QUANTUM ESPRESSO package [50,51], together with an in-house developed code (not publicly available currently). We employed the GGA with the PBE exchange-correlation functional [37] revised for solids (PBEsol) [52], in combination with the scalar relativistic optimized norm-conserving Vanderbilt pseudopotentials from the PseudoDojo set [53]. We considered 25/11/16/3 valence electrons for Lu, Y, Ru, and B, respectively. Plane-wave energy cutoffs of 100 Ry for the wavefunctions and 1000 Ry for the density were chosen, along with a Methfessel-Paxton smearing [54] of 0.010 Ry. We computed the band-resolved superfluid weight with a $9 \times 9 \times 14$ self-consistent **k**-point grid with 100 points along each path segment in the non-self-consistent calculation. The total superfluid weight required a non-self-consistent **k**-point grid of $63 \times 63 \times 98$ for convergence.

B. Electronic band structure

To rationalize the suppression of T_c in YRu_3B_2 and $LuRu_3B_2$ compared with $LaRu_3Si_2$ from an electronic-structure perspective, we compare their band structures (see Fig. 7). As the lattice constants contract from La to Y and Lu (Table II), the bands become more dispersive, most notably the quasiflat band near E_F from the Ru $d_{x^2-y^2}$ orbital (i.e., the red bands in Fig. 7 on the $k_z = 0$ plane). In $LaRu_3Si_2$, this quasiflat band spans ∼0.3 eV [14], whereas in YRu_3B_2 and $LuRu_3B_2$ its bandwidth increases to ∼0.7 eV (Fig. 7). This broadening substantially reduces the density of states (DOS) near E_F: The quasiflat band contribution decreases from 1.589 states/eV per spin in $LaRu_3Si_2$ to 0.754 states/eV per spin in YRu_3B_2 and 0.753 states/eV/spin in $LuRu_3B_2$, and the total DOS decreases from 5.308 states/eV per spin in La to 3.541 states/eV per spin in Y and 3.535 states/eV per spin in Lu. In contrast, the Ru d_{xz} DOS increases from 0.808 states/eV per spin in La to 1.125 states/eV per spin in Y and 1.123 states/eV per spin in Lu (listed in Table II). Here, all orbital labels refer to the local coordinate system defined in Refs. [14,43,44]. Since the EPC constant scales with the DOS as

$$\lambda = 2\frac{D(\mu)}{N}\frac{\hbar\langle g^2\rangle}{\hbar^2\langle\omega^2\rangle}, \tag{9}$$

where $\langle g^2\rangle$ is the Fermi surface averaged EPC strength, N is the number of unit cell, $D(\mu)$ is the DOS at chemical potential μ, and $\langle\omega^2\rangle$ is the McMillan average phonon frequency, the reduced $D(\mu)$ directly weakens EPC strength in YRu_3B_2 and $LuRu_3B_2$. This trend is consistent with recent experimental results on YRu_3Si_2 [55], where replacing La by the smaller Y ion reduces the in-plane lattice constant a from 5.715 to 5.472 Å and T_c from 6.8 to 3.4 K. Orbital-resolved band analysis further shows that, in RRu_3B_2 (R = Y, Lu), the Ru $d_{x^2-y^2}$-derived quasiflat band does not show an effective hole doping relative to $LaRu_3Si_2$. Instead, the Ru d_{xz} and d_{z^2} bands shift upward and become hole doped (Fig. 7). Moreover, the d_{z^2}-derived band lies substantially higher in energy (green bands in Fig. 7), which weakens the d_{z^2}-bonding-driven structural instability toward the $Cccm$ (orthorhombically distorted) phase [56].

TABLE II. Lattice constants (in unit of Å) after full relaxation, total (and orbital-projected) DOS at the Fermi level (in unit of states/eV per spin), and electron-phonon coupling constant $\lambda_{\text{e-ph}}$ for YRu_3B_2, $LuRu_3B_2$, and $LaRu_3Si_2$.

	YRu_3B_2	$LuRu_3B_2$	$LaRu_3Si_2$
a	5.5037	5.4762	5.7154
c	3.0267	3.0144	3.5755
$D(E_F)$ (total)	3.535	3.541	5.308
$D(E_F)(d_{x^2-y^2})$	0.754	0.753	1.589
$D(E_F)(d_{xz})$	1.125	1.123	0.808
$\lambda_{\text{e-ph}}$	0.477	0.561	0.831

C. Phonons and electron-phonon coupling

To assess phononic effects in RRu_3B_2 (R = Y, Lu) and benchmark against $LaRu_3Si_2$, we compute phonon dispersions within DFPT and analyze their mode character and contribution to the EPC. Relative to $LaRu_3Si_2$, the phonon spectra of RRu_3B_2 (see Fig. 8) are overall shifted to higher energies, consistent with the smaller atomic mass of B with respect to Si, the smaller lattice constants, and stiffer effective force constants. This increases the characteristic phonon scale $\langle\omega^2\rangle$ and therefore tends to reduce the EPC constant λ for comparable $\langle g^2\rangle$, particularly for the coupling between Ru $d_{x^2-y^2}$ states and Ru in-plane x modes.

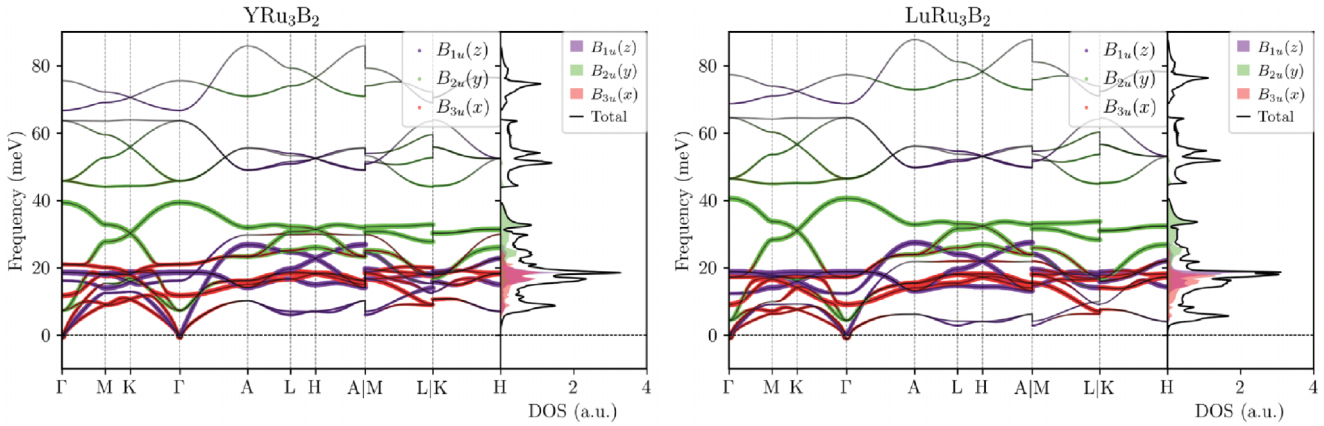

FIG. 8. Mode-projected phonon band structure and density of states of the $P6/mmm$ structure for YRu_3B_2 (left panel) and $LuRu_3B_2$ (right panel). The phonon modes (defined in local coordinates) of Ru atoms are projected onto the phonon band structure, with the radius of the circles proportional to the projected weight.

In $LuRu_3B_2$, we additionally identify a low-frequency branch at Γ dominated by Lu in-plane (xy) motion that becomes soft (see Fig. 8). The corresponding two-dimensional mode transforms as Γ_6^- and is compatible with a symmetry lowering to $Amm2$ (No. 38) (the representation follows the convention on the Bilbao Crystallographic Server [57–59]), i.e., a possible C_3-breaking distortion at low temperature. To avoid an artificial enhancement of λ associated with an incipient instability within harmonic EPC theory, we evaluate EPC using the stable phonon spectrum obtained at relatively larger electronic smearing, yielding $\lambda \simeq 0.561$ (Fig. 9) and an estimated $T_c \simeq 3.27$ K from the Allen-Dynes modified McMillan equation [60–62] with $\mu^* = 0.1$ for $LuRu_3B_2$. For YRu_3B_2, we obtain $\lambda \simeq 0.477$ and $T_c \simeq 1.88$ K. For reference, $T_c \simeq 6.8$ K reported in Ref. [14] was obtained using coarser **k** and **q**-point meshes in a high-throughput workflow (see Table S1 of the Supplemental Material [26] for a comparison). The theoretical values of λ with increased value for the smearing are close to the estimates based on experiments, namely, $\lambda_{\text{e-ph}}^{\text{exp}} = 0.41$ (for YRu_3B_2) and 0.45 (for $LuRu_3B_2$) (see Table I). It is worth noting that matching the experimental T_c within the Allen-Dynes framework requires $\mu^* \approx 0.14$ for Y and $\mu^* \approx 0.17$ for Lu. The mode-projected phonon DOS and the phonon dispersions in Fig. 8 show that the Ru in-plane x mode lies systematically below the corresponding y modes, mirroring the trend in $LaRu_3Si_2$. As we show below and in Fig. 9, this low-frequency Ru-x branch provides the dominant contribution to λ.

To quantify the microscopic EPC, we project the *ab initio* EPC tensor into a Wannier basis using EPW [46–49]. The leading real-space EPC matrix elements between Ru $d_{x^2-y^2}$ electrons and Ru x phonons are essentially the same for both YRu_3B_2 (0.02024 Ry/bohr), $LuRu_3B_2$ (0.02073 Ry/bohr), and $LaRu_3Si_2$ (0.02043 Ry/bohr). Given that the DOS at E_F from Ru d_{xz} and $d_{x^2-y^2}$ orbitals is comparable (Table II), we also evaluate the corresponding EPC elements for Ru d_{xz} electrons coupled to Ru x phonons, obtaining 0.01254 (Y), 0.01231 (Lu), and 0.00925 (La). With a matrix element roughly half as large and similar DOS, Eq. (9) implies that the d_{xz} channel contributes at the level of ∼1/4 of the $d_{x^2-y^2}$ channel, leaving the $d_{x^2-y^2}$ states as the dominant contributor to the total λ as in $LaRu_3Si_2$ [14]. Taken together, the near invariance of these real-space EPCs indicates that the reduced λ in RRu_3B_2 originates from the suppressed $d_{x^2-y^2}$ DOS and the overall hardening of the phonon spectrum.

We further examine the EPC-driven superconducting properties by calculating and analyzing the superconducting gap function projected onto the Fermi surfaces. Using the

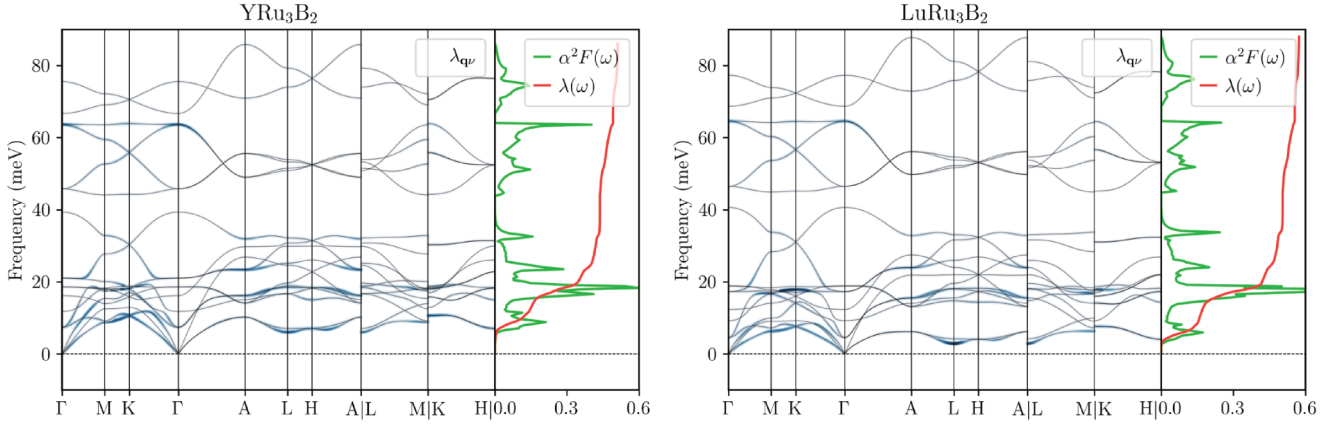

FIG. 9. Phonon band structure, Eliashberg spectral function $\alpha^2F(\omega)$, and electron-phonon coupling constant $\lambda(\omega)$ for YRu_3B_2 (left) and $LuRu_3B_2$ (right).

EPW package, we compute the anisotropic Eliashberg gaps for YRu_3B_2 and $LuRu_3B_2$ at $T = 0.1$ K. The calculated momentum- and band-resolved gap function $\Delta_{n\mathbf{k}}$ exhibits a clear multigap structure: A dominant gap of ∼0.8 meV opens on the Fermi-surface sheets with primarily Ru $d_{x^2-y^2}$ character (see the Supplemental Material [26] for details), whereas the Ru d_{xz}-derived sheets host a much smaller gap of ∼0.1 meV. This separation of gap scales in $R\mathrm{Ru}_3\mathrm{B}_2$ is similar to $\mathrm{LaRu}_3\mathrm{Si}_2$ and is consistent with a pairing mechanism controlled by the same mode-selective EPC channel [14]. Despite the similar gap anisotropy, the superconducting transition temperature is strongly reduced from ∼7 K in $\mathrm{LaRu}_3\mathrm{Si}_2$ to ∼1 K in $R\mathrm{Ru}_3\mathrm{B}_2$. Within an EPC picture, the T_c reduction is consistent with the broadening of the Ru $d_{x^2-y^2}$ quasiflat band under lattice contraction, which lowers the DOS at E_F and is expected to weaken λ accordingly. An instructive comparison can be made with the mean-field tight-binding pairing analysis (Sec. III D). There, assuming the same pairing interaction for all orbitals, the DOS differences lead to a slightly larger gap on the d_{xz}-derived sheets than on the $d_{x^2-y^2}$ sheets. In contrast, our first-principles Eliashberg results show that the $d_{x^2-y^2}$ gap dominates. This mismatch indicates that the pairing interaction is orbital dependent.

D. Mean-field tight-binding model analysis of the superconducting order parameter structure

We construct a tight-binding model from DFT by generating Wannier functions for the two kagome compounds. Using this model, we perform self-consistent mean-field superconductivity calculations following the approach described in Ref. [14], with an on-site attractive interaction applied uniformly to each orbital. This calculation yields superconducting order parameters for all 32 orbitals, revealing the relative contribution of different atoms and orbitals to superconductivity. The interaction strength is chosen to produce superconducting gaps consistent with the experimental T_c. We verified that the qualitative trends described below remain robust across a range of interaction values.

In both YRu_3B_2 and $LuRu_3B_2$, we find that the three d_{xz} orbitals of Ru have the same and the largest order parameter. Of the other contributions, the Ru $d_{x^2-y^2}$, d_{yz}, and d_{xy} orbitals (three each) are within the same order of magnitude as the Ru d_{xz} one. The contributions from the remaining Ru orbitals (s and d_{z^2}), and all Lu and B orbitals, are one or more orders of magnitude smaller. Superconductivity is thus primarily caused by pairing related to the orbitals of the Ru atoms that form the kagome structure. Here, it is interesting to note that DFT analysis of superconductivity for $\mathrm{LaRu}_3\mathrm{Si}_2$ found the Ru $d_{x^2-y^2}$ orbital to also dominate the superconducting order parameter [14]. However, the orbital content of the pairing gap differs because of the dominant density of states from $d_{x^2-y^2}$ close to Fermi level in $\mathrm{LaRu}_3\mathrm{Si}_2$, while in YRu_3B_2 and $LuRu_3B_2$ d_{xz} and $d_{x^2-y^2}$ contribute similarly to the density of states, as shown in Fig. 7. Our mean-field description reflects mainly the density of states, as the interaction is assumed uniform for all orbitals; for a more refined calculation, the orbital dependence of interactions as well as possible nearest-neighbor interactions would be needed. The DFT calculations in Sec. III C show that the gaps are different for different orbitals and the one of $d_{x^2-y^2}$ orbital is the largest; i.e., the density of states alone does not determine pairing.

E. Superfluid weight and penetration depth calculations

We calculate the superfluid weight (superfluid stiffness) tensor $D_s = D_{\mathrm{geom}} + D_{\mathrm{conv}}$, including both the conventional contribution D_{conv}, proportional to the band dispersion, and the geometric one D_{geom}, arising from the quantum geometry of the bands [18,63]. To simplify the computations, we utilize the zero-temperature formula for the superfluid weight, which assumes uniform pairing [64] (i, j are the Cartesian coordinates x, y, z):

$$D^{ij}_{\mathrm{conv}} = \frac{1}{V}\sum_{\mathbf{k}m}\frac{\Delta^2}{\sqrt{\epsilon_m^2+\Delta^2}^3}\partial_i\epsilon_m\partial_j\epsilon_m, \tag{10}$$

$$D^{ij}_{\mathrm{geom}} = \frac{1}{V}\sum_{\mathbf{k},m,n\neq m}\frac{\epsilon_n-\epsilon_m}{\epsilon_m+\epsilon_n}\left[\frac{\Delta^2}{\sqrt{\epsilon_m^2+\Delta^2}}-\frac{\Delta^2}{\sqrt{\epsilon_n^2+\Delta^2}}\right] \times(\langle\partial_i m|n\rangle\langle n|\partial_j m\rangle + \mathrm{H.c.}). \tag{11}$$

Here, ϵ_m is the energy dispersion shifted by the Fermi level, and it is a function of momentum $\mathbf{k}$ with m as the band index. The energy dispersions as well as the Bloch functions $|m\rangle$ and their derivatives are obtained by DFT. The superconducting gap Δ is estimated from the experimental T_c via the BCS relation $\Delta \simeq 1.76T_c$, which gives $\Delta = 0.106$ meV for the Y and 0.147 meV for the Lu compound. The values for the superfluid weight components are summarized in Table III. Our calculations reveal that the superfluid weight in these compounds is dominated by the conventional contribution. This is expected given the dispersive nature of bands near the Fermi level and that quantum geometric contributions become significant only when the pairing gap is comparable to or exceeds the bandwidth, which is not the case here. The conventional contribution is essentially insensitive to the value of the gap, as it is dominated by the band dispersion near the Fermi level rather than the magnitude of the pairing scale. In contrast, the geometric contribution exhibits a strong dependence on the superconducting gap. Increasing the gap to 2 meV enhances the geometric term by approximately two orders of magnitude. Nevertheless, the geometric contribution remains negligible compared to the conventional term.

To gain insight into which parts of the band structure contribute to the superfluid weight the most, we investigate the superfluid weight integrand $D_s^{ij}(\mathbf{k}, m)$ when the total superfluid weight is $D_s^{ij} = \sum_{\mathbf{k},m} D_s^{ij}(\mathbf{k}, m)$ [see Eqs. (10) and (11)]. Figure 10 shows the diagonal components of the superfluid weight integrand. The largest contributions for the xx and yy of the superfluid weight integrand components are found along the Γ–M–K–Γ and A–L–H–A lines, while the zz component vanishes on these planes. Conversely, D^{zz}_{conv} is nonzero only along the Γ–A, M–L, and K–H lines, where D^{xx}_{conv} and D^{yy}_{conv} vanish. This anisotropy follows from symmetry constraints and the fact that D_{conv} is directly proportional to the band dispersion. The crystal belongs to space group $P6/mmm$ (No. 191), which contains mirror planes perpendicular to k_x, k_y, and k_z passing through Γ, as well as mirror planes containing the A–L–H and K–M–L–H paths set by the translational symmetries. These mirror symmetries force the

TABLE III. Overview of total superfluid weight components computed from DFT data of YRu_3B_2 and $LuRu_3B_2$ with the uniform pairing assumption, and London penetration depths obtained from them. The calculation was done with $\Delta = 0.106$ meV (Y) and 0.147 meV (Lu).

Compound	$xy\lambda_L^{\text{th}}$ (nm)	$z\lambda_L^{\text{th}}$ (nm)	D_s^{xx} (1/H·m)	D_s^{yy} (1/Hm)	D_s^{zz} (1/Hm)	D_{conv}^{xx} (1/Hm)	D_{conv}^{yy} (1/Hm)	D_{conv}^{zz} (1/Hm)	D_{geom}^{xx} (1/Hm)	D_{geom}^{yy} (1/Hm)	D_{geom}^{zz} (1/Hm)
YRu_3B_2	32	24	7.8×10^{20}	7.8×10^{20}	1.4×10^{21}	7.8×10^{20}	7.8×10^{20}	1.4×10^{21}	2.6×10^{16}	2.6×10^{16}	1.8×10^{17}
$LuRu_3B_2$	36	26	6.2×10^{20}	6.2×10^{20}	1.4×10^{21}	6.2×10^{20}	6.2×10^{20}	1.4×10^{21}	6.3×10^{15}	6.3×10^{15}	1.1×10^{16}

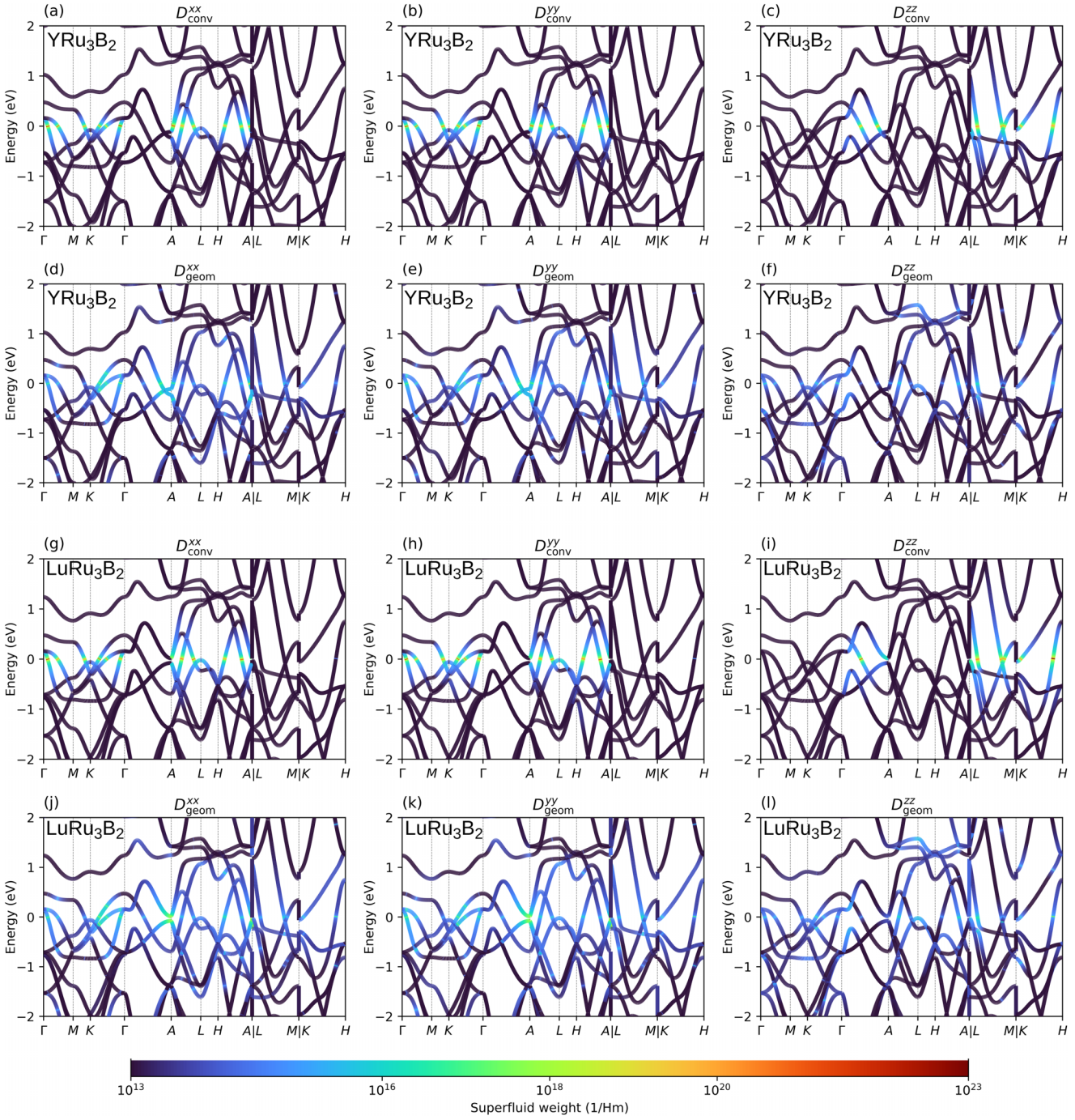

FIG. 10. Integrands $D^{ij}(\mathbf{k}, m)$ of the superfluid weight tensor components for YRu_3B_2 in the first two rows and $LuRu_3B_2$ in the last two, calculated using Eqs. (10) and (11) and DFT data, with $\Delta = 0.106$ meV (Y) and 0.147 meV (Lu). The conventional contribution is larger and concentrated on the Fermi energy, while the geometric is smaller and more spread out. Note that the colorscale is logarithmic.

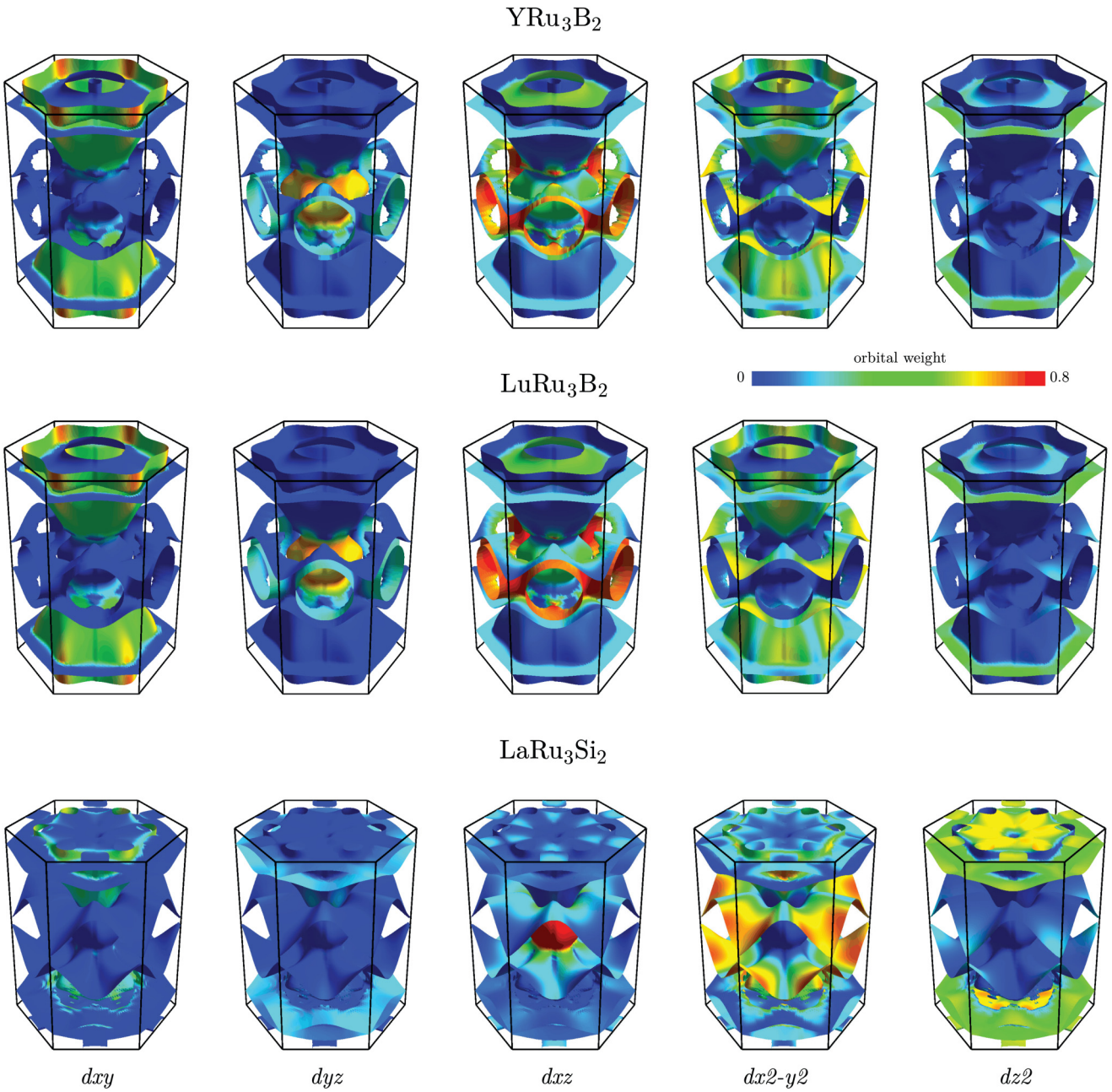

FIG. 11. Orbital-resolved Fermi surfaces of YRu_3B_2, $LuRu_3B_2$, and $LaRu_3Si_2$ in $P6/mmm$ phase, with the color denoting the orbital weight of Ru d orbitals in local coordinate.

component of the band dispersion normal to a mirror plane to vanish at mirror-invariant points. Thus, the dispersion along k_z is forbidden in Γ–M–K and A–L–H planes, while the $k_{x,y}$ one is suppressed along Γ–A, M–L, and K–H lines. To be precise, along the H–K line, only the xx component is forced to be zero by symmetry arguments. However, the zero dispersion along this direction, together with the other two nondispersive directions related by the C_{3z} symmetry, hinders the possibility of a large yy dispersion, as shown in Fig. 10.

The London penetration depth λ_L is related to the superfluid weight by

$$\lambda_L = (\mu_0 D_s)^{-1/2}. \tag{12}$$

We use this formula with D_s^{ii} to give the penetration depths λ_z^{th} in the $i = z$ direction and λ_{xy}^{th} in the $i = x, y$ directions, which are nearly identical due to the approximate xy isotropies of the system (see Fig. 11), even when the system is not xy symmetric. The penetration depth predictions are summarized in Table I. The calculations show that YRu_3B_2 has slightly smaller penetration depths than $LuRu_3B_2$; however, the error range partially overlaps. Both show a larger penetration depth in the xy plane compared to the z direction.

IV. CONCLUSIONS

We report the discovery of two superconductors, YRu_3B_2 and $LuRu_3B_2$, both predicted through ML-accelerated

high-throughput screening of kagome lattice materials. These compounds crystallize in the hexagonal $CeCo_3B_2$-type structure with planar Ru kagome networks and exhibit bulk superconductivity confirmed through magnetization, specific heat, and resistivity measurements with superconducting volume fractions close to 100%.

The experimental realization of these materials validates the predictive power of combining ML with first-principles calculations for superconductor discovery, even though the observed critical temperatures are lower than initially predicted. Our theoretical analysis explains this discrepancy through the incipient phase transition leading to an excessive softening of phonon modes in the calculations.

The contraction of lattice parameters from $LaRu_3Si_2$ to the smaller Y and Lu analogs increases band dispersion, particularly for the quasiflat kagome band derived from Ru $d_{x^2-y^2}$ orbitals. This enhanced dispersion reduces the density of states near the Fermi level, directly weakening the electron-phonon coupling constant and consequently suppressing T_c. Detailed phonon and Wannier-resolved EPC analysis shows that the dominant coupling channel remains the Ru $d_{x^2-y^2}$ states interacting with the low-frequency in-plane Ru-x branch, and its leading real-space matrix elements are nearly unchanged across the three compounds. The d_{xz} and $d_{x^2-y^2}$ orbitals have similar densities of states near the Fermi level. This shift in orbital character reflects the band structure reorganization accompanying lattice contraction, with d_{xz} and d_{z^2} bands becoming hole doped while the $d_{x^2-y^2}$ band remains near its original filling. Our mean-field analysis of the gaps, assuming uniform interaction for all orbitals, reflects the density of states and gives comparable gaps for both d_{xz} and $d_{x^2-y^2}$ orbitals. However, the more microscopic DFT calculations reveal a two-gap behavior with the larger gap for the $d_{x^2-y^2}$ orbital.

Our superfluid weight calculations demonstrate that conventional contributions dominate over quantum geometric effects in these materials. This is expected as quantum geometric contributions become significant only when the pairing gap is comparable to or exceeds the bandwidth, a condition not met in YRu_3B_2 and $LuRu_3B_2$. The calculated London penetration depths show moderate anisotropy between in-plane and out-of-plane directions, reflecting the quasi-two-dimensional character of the kagome structure.

The successful prediction-to-realization pipeline demonstrated here, from ML screening through first-principles calculations to experimental synthesis and characterization, represents a significant advance in accelerating superconductor discovery. While the materials space of the 1:3:2 kagome family is manageable with current computational methods, this integrated approach becomes increasingly valuable when extended to larger materials spaces where exhaustive first-principles calculations are prohibitively expensive. The key is the strategic combination of rapid ML-based prescreening to identify promising candidates, followed by targeted high-accuracy calculations and experimental investigation of the most viable predictions.

The broader significance of this work extends beyond these specific compounds. It provides a demonstration that the century-old paradigm of serendipitous superconductor discovery can be complemented, and in some cases replaced, by systematic, computation-guided materials design. As ML models improve and computational resources expand, this approach will become increasingly powerful for navigating the vast materials space and identifying superconductors with tailored properties. The successful realization of YRu_3B_2 and $LuRu_3B_2$ is a step toward this future, where theory, computation, and experiment work in concert to accelerate the discovery and characterization of quantum materials.

ACKNOWLEDGMENTS

This work was supported by a collaboration between The Kavli Foundation, Klaus Tschira Stiftung, and Kevin Wells, and by the Jane and Aatos Erkko Foundation, the Keele Foundation, and the Magnus Ehrnrooth Foundation, as part of the SuperC collaboration. B.A.B., M.A.L.M., and P.T. were supported by a grant from the Simons Foundation (SFI-MPS-NFS-00006741-01, B.A.B.; SFI-MPS-NFS-00006741-13, M.A.L.M.; SFI-MPS-NFS-00006741-12, P.T.) in the Simons Collaboration on New Frontiers in Superconductivity. B.A.B. was also supported by the Gordon and Betty Moore Foundation through Grant No. GBMF8685 toward the Princeton theory program, the Gordon and Betty Moore Foundation's EPiQS Initiative (Grant No. GBMF11070), the Office of Naval Research (ONR Grant No. N00014-20-1-2303), the Global Collaborative Network Grant at Princeton University, the Simons Investigator Grant No. 404513, the NSF-MERSEC (Grant No. MERSEC DMR 2011750), Princeton Catalysis Initiative, the Schmidt Foundation at the Princeton University, and the National Science Foundation through the AI Research Institutes program Award No. DMR-2433348. Y.J. and partially B.A.B. were supported by a European Research Council (ERC) under the European Union's Horizon 2020 research and innovation program (Grant Agreement No. 101020833). This work is part of the Finnish Centre of Excellence in Quantum Materials (QMAT). We thank Kristjan Haule and Théo Cavignac for useful discussions. S.K.P. acknowledge the support from Rice university Smalley-Curl Institute through post-doctoral fellowship.

DATA AVAILABILITY

There are no publicly available research data or software supporting this manuscript. Requests for further information or data should be sent to the authors.

[1] M. Tinkham, *Introduction to Superconductivity*, 2nd ed. (McGraw-Hill, New York, 1996).

[2] J. Bardeen, L. N. Cooper, and J. R. Schrieffer, Theory of superconductivity, Phys. Rev. **108**, 1175 (1957).

[3] J. G. Bednorz and K. A. Müller, Possible high T_c superconductivity in the Ba-La-Cu-O system, Z. Phys. B **64**, 189 (1986).

[4] Y. Kamihara, T. Watanabe, M. Hirano, and H. Hosono, Iron-based layered superconductor La[$O_{1-x}F_x$]FeAs ($x = 0.05$–

0.12) with T_c = 26 K, J. Am. Chem. Soc. **130**, 3296 (2008).
[5] F. Steglich, J. Aarts, C. D. Bredl, W. Lieke, D. Meschede, W. Franz, and H. Schäfer, Superconductivity in the presence of strong Pauli paramagnetism: $CeCu_2Si_2$, Phys. Rev. Lett. **43**, 1892 (1979).
[6] M. R. D. Jérome, A. Mazaud, and K. Bechgaard, Superconductivity in a synthetic organic conductor (TMTSF)2PF_6, J. Phys. Lett. **41**, 95 (1980).
[7] D. Li, K. Lee, B. Y. Wang, M. Osada, S. Crossley, H. R. Lee, Y. Cui, Y. Hikita, and H. Y. Hwang, Superconductivity in an infinite-layer nickelate, Nature (London) **572**, 624 (2019).
[8] D. Li, K. Lee, B. Y. Wang, M. Osada, S. Crossley, H. R. Lee, Y. Cui, Y. Hikita, and H. Y. Hwang, Superconductivity at 39 K in magnesium diboride, Nature (London) **410**, 432 (2001).
[9] N. W. Ashcroft, Metallic hydrogen: A high-temperature superconductor? Phys. Rev. Lett. **21**, 1748 (1968).
[10] N. W. Ashcroft, Hydrogen dominant metallic alloys: High temperature superconductors? Phys. Rev. Lett. **92**, 187002 (2004).
[11] L. Boeri, R. G. Hennig, P. J. Hirschfeld, G. Profeta, A. Sanna, E. Zurek, W. E. Pickett, M. Amsler, R. Dias, M. Eremets, *et al.*, The 2021 room-temperature superconductivity roadmap, J. Phys.: Condens. Matter **34**, 183002 (2022).
[12] K. Gao, T. Cerqueira, A. Sanna, Y.-W. Fang, Đ. Dangić, I. Errea, H.-C. Wang, S. Botti, and M. A. L. Marques, The maximum T_c of conventional superconductors at ambient pressure, Nat. Commun. **16**, 8253 (2025).
[13] J. B. Gibson, A. C. Hire, P. Prakash, P. M. Dee, B. Geisler, J. S. Kim, Z. Li, J. J. Hamlin, G. R. Stewart, P. J. Hirschfeld, and R. G. Hennig, Developing a complete AI-accelerated workflow for superconductor discovery, npj Comput. Mater. **12**, 95 (2025).
[14] J. Deng, Y. Jiang, T. F. T. Cerqueira, H. Hu, E. O. Lamponen, D. Călugăru, Z. W. Hanqi Pi, M. G. Vergniory, E. Morosan, T. Neupert, S. Blanco-Canosa, C. Felser, K. Haule, M. A. L. Marques, P. Törmä, and B. A. Bernevig, Theory of superconductivity in $LaRu_3Si_2$ and predictions of new kagome flat band superconductors, arXiv:2503.20867.
[15] P. Prakash, J. B. Gibson, Z. Li, G. D. Gianluca, J. Esquivel, E. Fuemmeler, B. Geisler, J. S. Kim, A. Roitberg, E. B. Tadmor, M. Liu, S. Martiniani, G. R. Stewart, J. J. Hamlin, P. J. Hirschfeld, and R. G. Hennig, Guided diffusion for the discovery of new superconductors, arXiv:2509.25186.
[16] O. Lesser, Y. Liu, N. Maus, A. Panigrahi, K. Mallayya, A. Gong, A. Kabra, S. B. Lee, S. Chatterjee, A. Merino, K. Q. Weinberger, L. M. Schoop, J. R. Gardner, and E.-A. Kim, Electron affinity difference distributions guide the discovery of the superconductor $PtPb_3Bi$, arXiv:2510.07373.
[17] J. Yu, B. A. Bernevig, R. Queiroz, E. Rossi, P. Törmä, and B.-J. Yang, Quantum geometry in quantum materials, npj Quantum Mater. **10**, 101 (2025).
[18] S. Peotta and P. Törmä, Superfluidity in topologically nontrivial flat bands, Nat. Commun. **6**, 8944 (2015).
[19] P. Törmä, S. Peotta, and B. A. Bernevig, Superconductivity, superfluidity and quantum geometry in twisted multilayer systems, Nat. Rev. Phys. **4**, 528 (2022).
[20] H. Hu, O. Vafek, K. Haule, and B. A. Bernevig, Ferromagnetism vs. antiferromagnetism in narrow-band systems: Competition between quantum geometry and band dispersion, arXiv:2509.03575.
[21] T. Gaggl, R. Misawa, M. Kriener, Y. Tanaka, R. Yamada, and M. Hirschberger, Bulk superconductivity in the kagome metal YRu_3B_2, Phys. Scr. **101**, 055912 (2026).
[22] M. J. Winiarski, D. Walczak, S. Królak, D. Yazici, R. J. Cava, and T. Klimczuk, YRu_3B_2—A kagome lattice superconductor, J. Phys.: Mater. **9**, 025013 (2026).
[23] H. Ku, G. Meisner, F. Acker, and D. Johnston, Superconducting and magnetic properties of new ternary borides with the $CeCo_3B_2$-type structure, Solid State Commun. **35**, 91 (1980).
[24] K. Hiebl, P. Rogl, E. Uhl, and M. J. Sienko, Magnetic behavior and structural chemistry of $RERu_3B_2$ borides, Inorg. Chem. **19**, 3316 (1980).
[25] T. Roisnel and J. Rodríguez-Carvajal, Winplotr: A Windows tool for powder diffraction pattern analysis, Mater. Sci. Forum **378–381**, 118 (2001).
[26] See Supplemental Material at http://link.aps.org/supplemental/10.1103/lpqj-7hyg for detailed low temperature heat capacity data and calculations of the superconducting gap on the Fermi surface.
[27] L. L. Zhao, S. Lausberg, H. Kim, M. A. Tanatar, M. Brando, R. Prozorov, and E. Morosan, Type-I superconductivity in $YbSb_2$ single crystals, Phys. Rev. B **85**, 214526 (2012).
[28] C.-w. Cho, J. H. Yang, N. F. Q. Yuan, J. Shen, T. Wolf, and R. Lortz, Thermodynamic evidence for the Fulde-Ferrell-Larkin-Ovchinnikov state in the KFe_2As_2 superconductor, Phys. Rev. Lett. **119**, 217002 (2017).
[29] S. Ichinokura, Y. Nakata, K. Sugawara, Y. Endo, A. Takayama, T. Takahashi, and S. Hasegawa, Vortex-induced quantum metallicity in the mono-unit-layer superconductor $NbSe_2$, Phys. Rev. B **99**, 220501 (2019).
[30] R. Joynt and L. Taillefer, The superconducting phases of UPt_3, Rev. Mod. Phys. **74**, 235 (2002).
[31] D. Aoki, F. Honda, G. Knebel, D. Braithwaite, A. Nakamura, D. Li, Y. Homma, Y. Shimizu, Y. J. Sato, J. P. Brison, and J. Flouquet, Multiple superconducting phases and unusual enhancement of the upper critical field in UTe_2, J. Phys. Soc. Jpn. **89**, 053705 (2020).
[32] A. Rosuel, C. Marcenat, G. Knebel, T. Klein, A. Pourret, N. Marquardt, Q. Niu, S. Rousseau, A. Demuer, G. Seyfarth, G. Lapertot, D. Aoki, D. Braithwaite, J. Flouquet, and J. P. Brison, Field-induced tuning of the pairing state in a superconductor, Phys. Rev. X **13**, 011022 (2023).
[33] P. E. Blöchl, Projector augmented-wave method, Phys. Rev. B **50**, 17953 (1994).
[34] G. Kresse and D. Joubert, From ultrasoft pseudopotentials to the projector augmented-wave method, Phys. Rev. B **59**, 1758 (1999).
[35] G. Kresse and J. Furthmüller, Efficiency of ab-initio total energy calculations for metals and semiconductors using a plane-wave basis set, Comput. Mater. Sci. **6**, 15 (1996).
[36] G. Kresse and J. Furthmüuller, Efficient iterative schemes for *ab initio* total-energy calculations using a plane-wave basis set, Phys. Rev. B **54**, 11169 (1996).
[37] J. P. Perdew, K. Burke, and M. Ernzerhof, Generalized gradient approximation made simple, Phys. Rev. Lett. **77**, 3865 (1996).
[38] H. J. Monkhorst and J. D. Pack, Special points for Brillouin-zone integrations, Phys. Rev. B **13**, 5188 (1976).
[39] J. Gao, Q. Wu, C. Persson, and Z. Wang, Irvsp: To obtain irreducible representations of electronic states in the VASP, Comput. Phys. Commun. **261**, 107760 (2021).

[40] A. A. Mostofi, J. R. Yates, Y.-S. Lee, I. Souza, D. Vanderbilt, and N. Marzari, Wannier90: A tool for obtaining maximally-localised Wannier functions, Comput. Phys. Commun. **178**, 685 (2008).

[41] A. A. Mostofi, J. R. Yates, G. Pizzi, Y.-S. Lee, I. Souza, D. Vanderbilt, and N. Marzari, An updated version of Wannier90: A tool for obtaining maximally-localised Wannier functions, Comput. Phys. Commun. **185**, 2309 (2014).

[42] G. Pizzi, V. Vitale, R. Arita, S. Blügel, F. Freimuth, G. Géranton, M. Gibertini, D. Gresch, C. Johnson, T. Koretsune, *et al.*, Wannier90 as a community code: New features and applications, J. Phys.: Condens. Matter **32**, 165902 (2020).

[43] J. Deng, R. Zhang, Y. Xie, X. Wu, and Z. Wang, Two elementary band representation model, Fermi surface nesting, and surface topological superconductivity in AV_3Sb_5 ($A = $ K, Rb, Cs), Phys. Rev. B **108**, 115123 (2023).

[44] Y. Jiang, H. Hu, D. Călugăru, C. Felser, S. Blanco-Canosa, H. Weng, Y. Xu, and B. A. Bernevig, FeGe as a building block for the kagome 1:1, 1:6:6, and 1:3:5 families: Hidden d-orbital decoupling of flat band sectors, effective models, and interaction Hamiltonians, Phys. Rev. B **111**, 125163 (2025).

[45] Q. Wu, S. Zhang, H.-F. Song, M. Troyer, and A. A. Soluyanov, WannierTools: An open-source software package for novel topological materials, Comput. Phys. Commun. **224**, 405 (2018).

[46] F. Giustino, M. L. Cohen, and S. G. Louie, Electron-phonon interaction using Wannier functions, Phys. Rev. B **76**, 165108 (2007).

[47] J. Noffsinger, F. Giustino, B. D. Malone, C.-H. Park, S. G. Louie, and M. L. Cohen, EPW: A program for calculating the electron–phonon coupling using maximally localized Wannier functions, Comput. Phys. Commun. **181**, 2140 (2010).

[48] S. Poncé, E. R. Margine, C. Verdi, and F. Giustino, EPW: Electron-phonon coupling, transport and superconducting properties using maximally localized Wannier functions, Comput. Phys. Commun. **209**, 116 (2016).

[49] H. Lee, S. Poncé, K. Bushick, S. Hajinazar, J. Lafuente-Bartolome, J. Leveillee, C. Lian, J.-M. Lihm, F. Macheda, H. Mori, H. Paudyal, W. H. Sio, S. Tiwari, M. Zacharias, X. Zhang, N. Bonini, E. Kioupakis, E. R. Margine, and F. Giustino, Electron-phonon physics from first principles using the EPW code, npj Comput. Mater. **9**, 156 (2023).

[50] P. Giannozzi, S. Baroni, N. Bonini, M. Calandra, R. Car, C. Cavazzoni, D. Ceresoli, G. L. Chiarotti, M. Cococcioni, I. Dabo, *et al.*, QUANTUM ESPRESSO: A modular and open-source software project for quantum simulations of materials, J. Phys.: Condens. Matter **21**, 395502 (2009).

[51] P. Giannozzi, O. Andreussi, T. Brumme, O. Bunau, M. Buongiorno Nardelli, M. Calandra, R. Car, C. Cavazzoni, D. Ceresoli, M. Cococcioni, *et al.*, Advanced capabilities for materials modelling with Quantum Espresso, J. Phys.: Condens. Matter **29**, 465901 (2017).

[52] J. P. Perdew, A. Ruzsinszky, G. I. Csonka, O. A. Vydrov, G. E. Scuseria, L. A. Constantin, X. Zhou, and K. Burke, Restoring the density-gradient expansion for exchange in solids and surfaces, Phys. Rev. Lett. **100**, 136406 (2008).

[53] M. Van Setten, M. Giantomassi, E. Bousquet, M. Verstraete, D. Hamann, X. Gonze, and G.-M. Rignanese, The PseudoDojo: Training and grading a 85 element optimized norm-conserving pseudopotential table, Comput. Phys. Commun. **226**, 39 (2018).

[54] M. Methfessel and A. T. Paxton, High-precision sampling for Brillouin-zone integration in metals, Phys. Rev. B **40**, 3616 (1989).

[55] P. Kràl, J. N. Graham, V. Sazgari, I. Plokhikh, A. Lukovkina, O. Gerguri, I. Bialo, A. Doll, L. Martinelli, J. Oppliger, *et al.*, Discovery of high-temperature charge order and time-reversal symmetry-breaking in the kagome superconductor YRu_3Si_2, arXiv:2507.06885.

[56] R. Misawa, S. Kitou, R. Yamada, T. Gaggl, R. Nakano, Y. Shibata, Y. Okamura, M. Kriener, P. R. Baral, Y. Nakamura, Y. Ōnuki, Y. Takahashi, T.-H. Arima, M. Jovanovic, L. M. Schoop, and M. Hirschberger, Successive orthorhombic distortions in kagome metals by molecular orbital formation, Adv. Mater. **38**, e13015 (2026).

[57] M. I. Aroyo, J. M. Perez-Mato, D. Orobengoa, E. Tasci, G. de la Flor, and A. Kirov, Crystallography online: Bilbao Crystallographic Server, Bulg. Chem. Commun. **43**, 183 (2011).

[58] M. I. Aroyo, J. M. Perez-Mato, C. Capillas, E. Kroumova, S. Ivantchev, G. Madariaga, A. Kirov, and H. Wondratschek, Bilbao Crystallographic Server: I. Databases and crystallographic computing programs, Z. Kristallogr. Cryst. Mater. **221**, 15 (2006).

[59] M. I. Aroyo, A. Kirov, C. Capillas, J. Perez-Mato, and H. Wondratschek, Bilbao Crystallographic Server. II. Representations of crystallographic point groups and space groups, Acta Crystallogr. A Found. Crystallogr. **62**, 115 (2006).

[60] W. L. McMillan, Transition temperature of strong-coupled superconductors, Phys. Rev. **167**, 331 (1968).

[61] R. Dynes, McMillan's equation and the T_c of superconductors, Solid State Commun. **10**, 615 (1972).

[62] P. B. Allen and R. C. Dynes, Transition temperature of strong-coupled superconductors reanalyzed, Phys. Rev. B **12**, 905 (1975).

[63] K.-E. Huhtinen, J. Herzog-Arbeitman, A. Chew, B. A. Bernevig, and P. Törmä, Revisiting flat band superconductivity: Dependence on minimal quantum metric and band touchings, Phys. Rev. B **106**, 014518 (2022).

[64] L. Liang, T. I. Vanhala, S. Peotta, T. Siro, A. Harju, and P. Törmä, Band geometry, Berry curvature, and superfluid weight, Phys. Rev. B **95**, 024515 (2017).